Supporting Information for

Unidirectional Spin-Orbit Interaction Induced by the Line Defect in Monolayer Transition Metal Dichalcogenides for High-Performance Devices

Xiaoyin Li,[†, §] Shunhong Zhang,[‡, §] Huaqing Huang,[§] Lin Hu,[§] Feng Liu[*,§] and Qian Wang[*,†]

[†]Center for Applied Physics and Technology, Department of Materials Science and Engineering, HEDPS, College of Engineering, Peking University, Beijing 100871, China

[‡]International Center for Quantum Design of Functional Materials (ICQD), Hefei National Laboratory for Physical Sciences at Microscale, University of Science and Technology of China, Hefei, Anhui 230026, China

[§]Department of Materials Science and Engineering, University of Utah, Salt Lake City, Utah 84112, United States

Analysis of high-order SOC terms in the $\boldsymbol{k} \cdot \boldsymbol{p}$ model

It has already been demonstrated that only odd order terms of $\boldsymbol{k}$ contribute to the effective SOC Hamiltonian in the presence of time reversal symmetry.[1, 2] Herein we start from the third-order polynomials of the $\boldsymbol{k} \cdot \boldsymbol{p}$ model to analyze the SOC in the DLD-I engineered WS_2. The point group symmetry of the DLD-I engineered WS_2 is C_2, having the character table as

Character table for C_2 point group

	E	C_2	linear, rotations
A	1	1	x, R_x
B	1	-1	y, z, R_y, R_z

Accordingly, $\boldsymbol{k}$ and $\boldsymbol{\sigma}$ can be sorted as two irreducible representations, i.e. A: k_x, σ_x; B: k_y, k_z, σ_y, σ_z, as stated in the main text. Then from the table of direct products of C_2 point group

Product table for C_2 point group

	A	B
A	A	B
B	B	A

one can further classify the third-order terms of $\boldsymbol{k}$ as A: k_x^3, $k_xk_yk_z$, $k_y^2k_x$, $k_z^2k_x$; B: k_y^3, k_z^3, $k_x^2k_y$, $k_x^2k_z$, $k_y^2k_z$, $k_z^2k_y$. However, due to the one-dimensional (1D) nature of

the defect states in the DLD-I engineered WS_2, all the terms containing k_y or k_z should vanish, leaving k_x^3 the only nonzero term. Its direct product with σ_x belongs to the total symmetric irreducible representation A, leading to the only possible third-order contribution to the SOC Hamiltonian: $k_x^3\sigma_x$. Applying this method to higher-order terms in $\boldsymbol{k}$, one obtains similar results. That is, for any odd order n in $\boldsymbol{k}$, the expanded nth-order polynomials only contain a single nonzero term k_x^n, and all the other terms vanish due to the 1D nature of the defect states which extend in the $\boldsymbol{x}$ direction. Moreover, the only combination of k_x^n with Pauli matrix that corresponds to the A irreducible representation is $k_x^n\sigma_x$. Therefore, the effective SOC Hamiltonian of the DLD-I engineered WS_2 in the $\boldsymbol{k}\cdot\boldsymbol{p}$ formalism up to the nth-order in $\boldsymbol{k}$ reads: $H_{so}(\boldsymbol{k}) = \alpha_1 k_x\sigma_x + \alpha_3 k_x^3\sigma_x + \alpha_5 k_x^5\sigma_x + ... + \alpha_n k_x^n\sigma_x$, where α_i represents the ith-order in $\boldsymbol{k}$ SOC parameter. It demonstrates that the nonzero spin component is always σ_x, no matter what the order of $\boldsymbol{k}$ is.

For the DLD-II engineered WS_2, similar analysis can be applied. Here the point group symmetry is C_s and the character table is

Character table for C_s point group

	E	S_y	linear, rotations
A'	1	1	x, z, R_y
A''	1	-1	y, R_x, R_z

As presented in the main text, $\boldsymbol{k}$ and $\boldsymbol{\sigma}$ can be sorted as A': k_x, k_z, σ_y; A'': k_y, σ_x, σ_z. Combining with the corresponding table of direct products

Product table for C_s point group

	A'	A''
A'	A'	A''
A''	A''	A'

one can classify the third-order terms of $\boldsymbol{k}$ as A': k_x^3, k_z^3, $k_x^2k_z$, $k_y^2k_x$, $k_y^2k_z$, $k_z^2k_x$; A'':

k_y^3, $k_x^2 k_y$, $k_x k_y k_z$, $k_z^2 k_y$. Because of the 1D nature of the defect states in the DLD-II engineered WS_2, all the terms that contain k_y and k_z should vanish and the only nonzero term is k_x^3, same as that in the DLD-I engineered WS_2. The combination of k_x^3 with Pauli matrix that belongs to the A' irreducible representation is $k_x^3\sigma_y$, which is the only possible third-order contribution to the SOC Hamiltonian. For the higher odd order n in $\boldsymbol{k}$, the only nonzero term is k_x^n. Its combination with Pauli matrix that corresponds to the A' irreducible representation is $k_x^n\sigma_y$, which is the only possible nth-order in $\boldsymbol{k}$ contributing to the SOC Hamiltonian. Therefore, the effective SOC Hamiltonian of the DLD-II engineered WS_2 in the $\boldsymbol{k}\cdot\boldsymbol{p}$ formalism up to the nth-order in $\boldsymbol{k}$ can be written as: $H_{so}(\boldsymbol{k}) = \alpha_1 k_x\sigma_y + \alpha_3 k_x^3\sigma_y + \alpha_5 k_x^5\sigma_y + ... + \alpha_n k_x^n\sigma_y$, where α_i represents the ith-order in $\boldsymbol{k}$ SOC parameter. It demonstrates that the nonzero spin component is always σ_y, no matter what the order of $\boldsymbol{k}$ is.

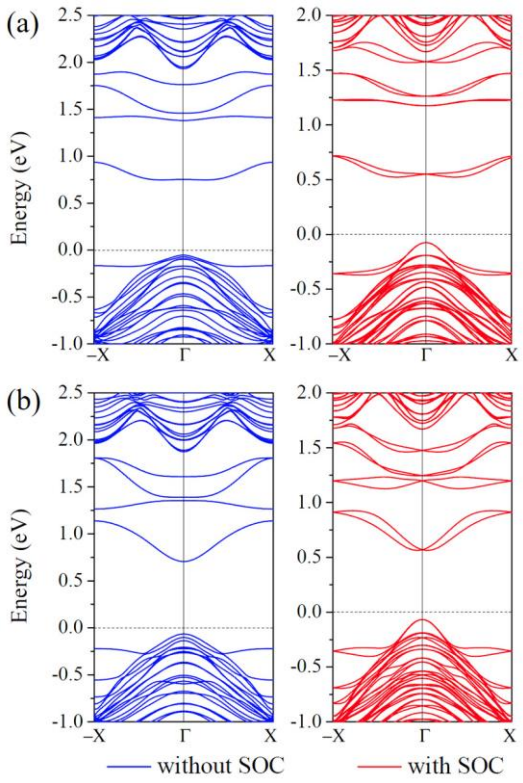

Figure S1. Band structures without and with SOC of (a) DLD-I and (b) DLD-II engineered WS_2, respectively, where the supercell size along the direction

perpendicular to the line defects is extended by ten times.

To assess the stability of the proposed DLDs, we calculate their formation energy, phonon dispersion of the ground state structure, and perform *ab initio* molecular dynamics simulation at 300 K. The formation energy of the DLDs in WS_2 systems is defined as $E_f = (E_{vac} + N\mu_S - E_{bulk})/N$. Here E_{bulk} and E_{vac} are the energies of the pristine and vacancy containing supercells, N is the number of S vacancies, and the chemical potential of S (μ_S) is taken as the energy of the isolated S atom, corresponding to removing S atoms from the monolayer to vacuum. The obtained formation energy of the DLD-I (DLD-II) is 5.997 (6.067) eV/vacancy. For comparison, we also calculate the formation energy of a single S vacancy, which is 6.020 eV/vacancy. Therefore, the formation energy of the proposed DLD is comparable to that of the single chalcogen vacancy, suggesting that the formation of the DLDs is energetically accessible.

We then calculate the phonon dispersion of the DLD engineered WS_2 to examine the dynamic stability. Figure S2 shows the calculated phonon spectra. One can see that there is no imaginary mode along all high symmetric paths for both the DLD-I and the DLD-II engineered WS_2, indicating that the introduction of the DLDs will not affect the dynamic stability of the structure. The dynamic stability also helps rule out the possibility of CDW modulation in these DLDs as has been discussed in the mirror twin boundary of $MoSe_2$.[3]

We also perform *ab initio* molecular dynamics simulations at 300 K to check the thermal stability of the DLD engineered WS_2. A 5×1×1 supercell containing 230 atoms is used. As shown in Figure S3, after heating 10 *ps* at 300 K the structure still keeps intact, indicating that the DLD engineered WS_2 is thermally stable at room temperature.

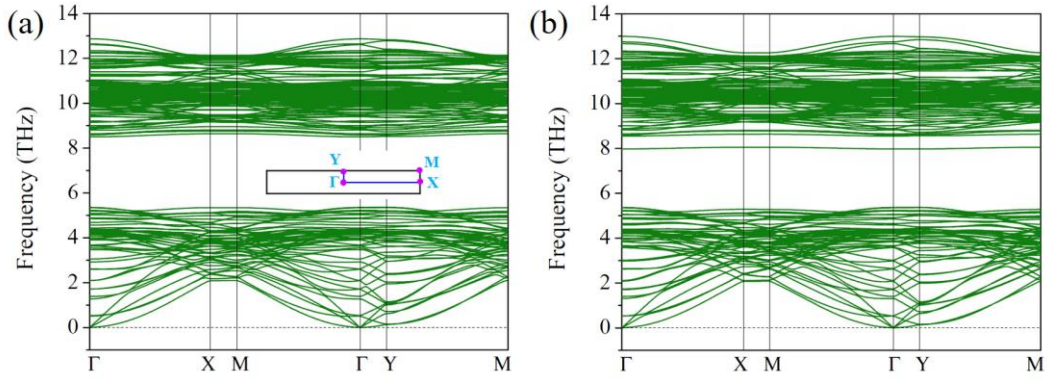

Figure S2. Phonon dispersion of (a) the DLD-I and (b) the DLD-II engineered WS_2. The inset in (a) illustrates the Brillouin zone and high symmetric points.

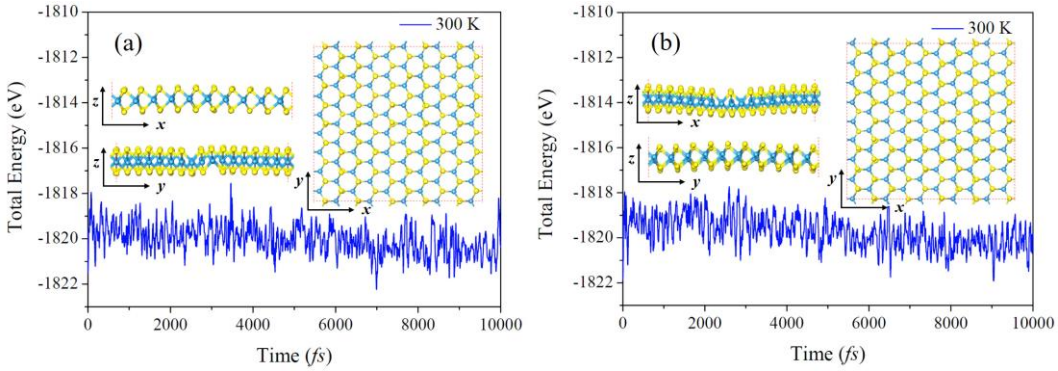

Figure S3. Fluctuations of total potential energy of (a) the DLD-I and (b) the DLD-II engineered WS_2 with time during the *ab initio* molecular dynamics simulations at 300 K. The insets are the snapshots of the structures at the end of the simulation.

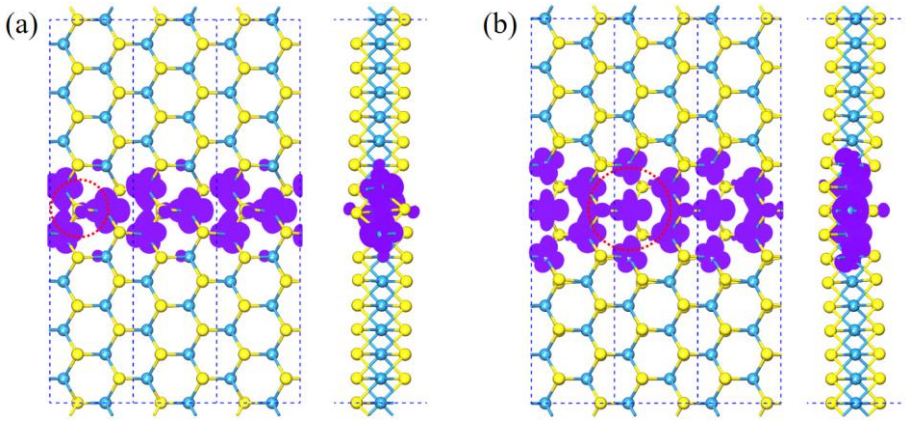

Figure S4. Charge density distribution for the conduction bands of (a) DLD-I and (b) DLD-II engineered WS_2, respectively. The isovalue is 0.03 $eÅ^{-3}$. The red circle represents the orbital that is used to construct the tight-binding model Hamiltonian.

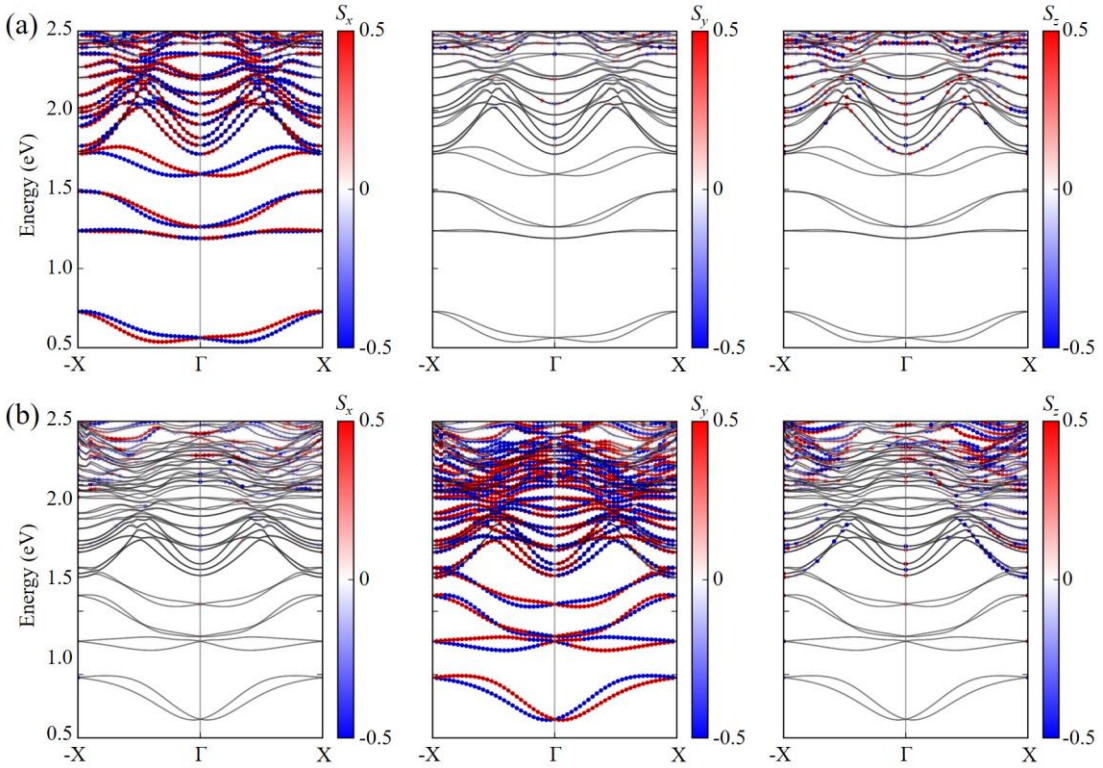

Figure S5. Spin-projected band structure of (a) DLD-I and (b) DLD-II engineered WS_2 similar to Figure 3 in the main text but in a larger energy window.

The band structures of the DLD engineered WS_2 along the ***y*** direction are calculated and summarized in Figure S6, where the conduction states are nearly dispersionless since the DLDs are isolated far from each other along this direction. When zooming in the energy window, some small dispersion and spin splitting appear because of the finite supercell size used along the ***y*** direction. One can see that the conduction states become completely dispersionless and spin degenerate when the supercell size along the ***y*** direction is increased to ~50 Å (see Figure S7). By analyzing the spin components along the Γ-Y direction, we found small nonzero S_y and S_z values for the DLD-I engineered WS_2 and nonzero S_x and S_z values for the DLD-II engineered WS_2 (Figure S8), which are consistent with the analyses of the $\boldsymbol{k} \cdot \boldsymbol{p}$ model in the main text. However, we should point out that the spin components emerging along the Γ-Y direction have marginal effect on the coherent spin transport, because spin splitting will disappear once the supercell size along this direction is large enough and the eigenstates with $k_y = 0$

momentum dominate the transport properties.

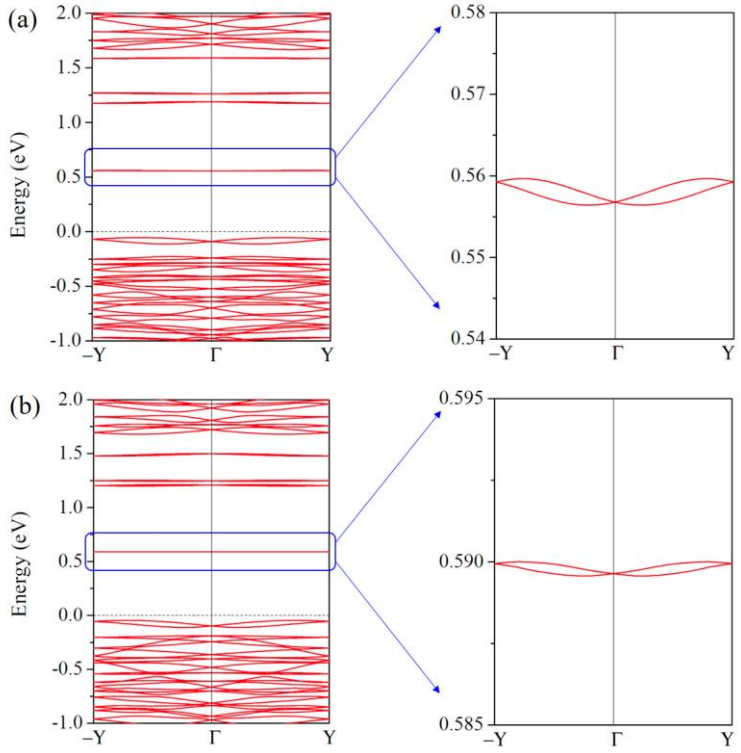

Figure S6. Band structures of (a) DLD-I and (b) DLD-II engineered WS_2 along the Γ-Y path with SOC.

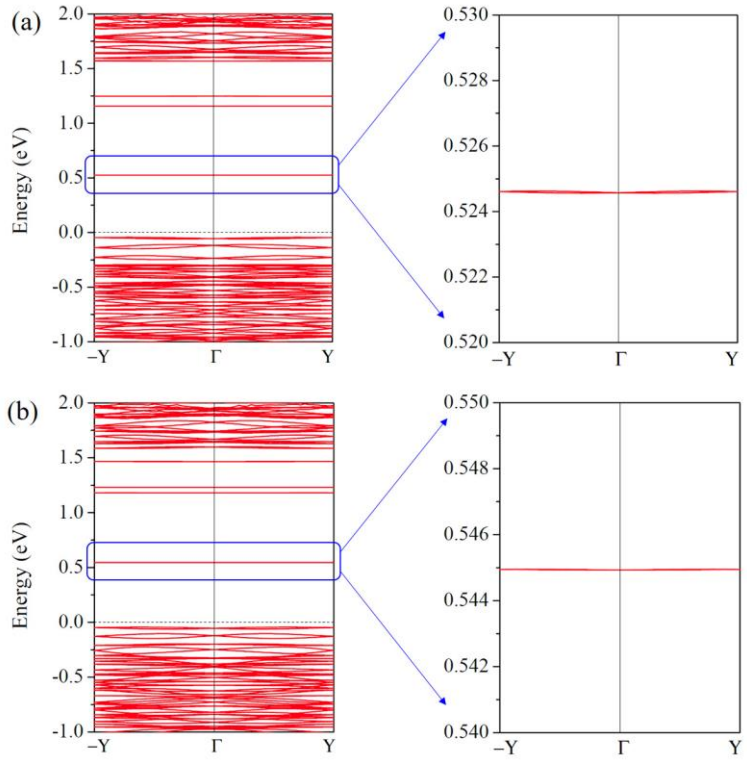

Figure S7. Band structures of (a) DLD-I and (b) DLD-II engineered WS_2 along the Γ-Y path with SOC, where the supercell size along the direction perpendicular to the line defects is extended by sixteen times (~50 Å).

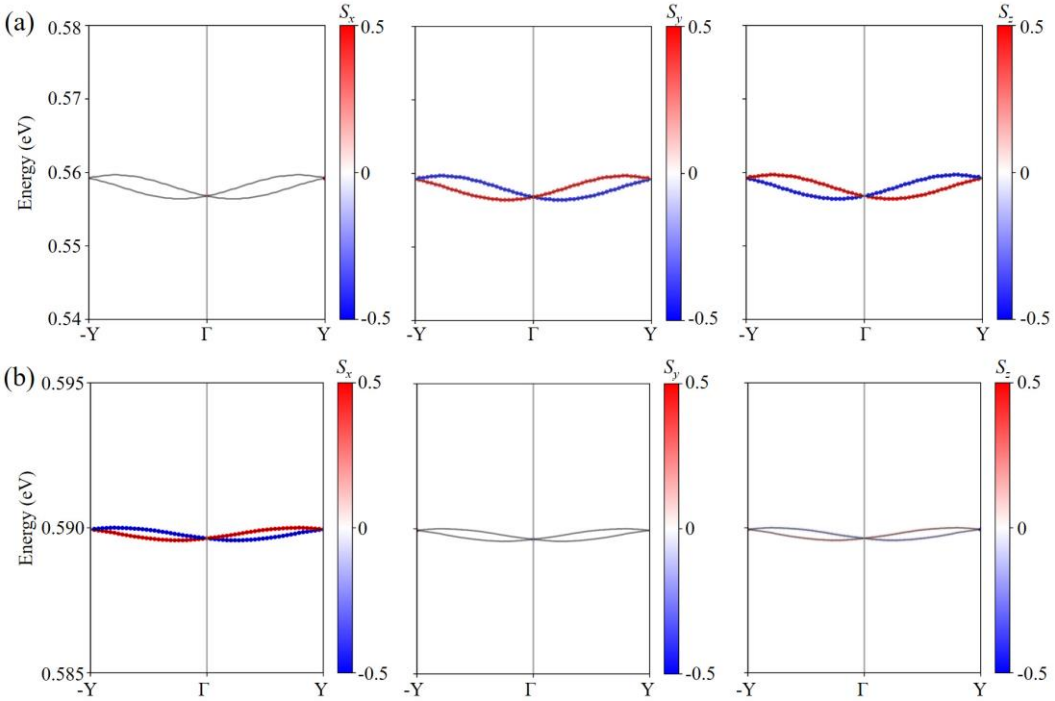

Figure S8. Spin-projected conduction bands of (a) DLD-I and (b) DLD-II engineered WS_2 along the Γ-Y path. The supercell size along the direction perpendicular to the line

defects is the same as that used in Figure 2 of the main text. In (b), although the value of S_z is much smaller than that of S_x, they are both nonzero along the Γ-Y path.

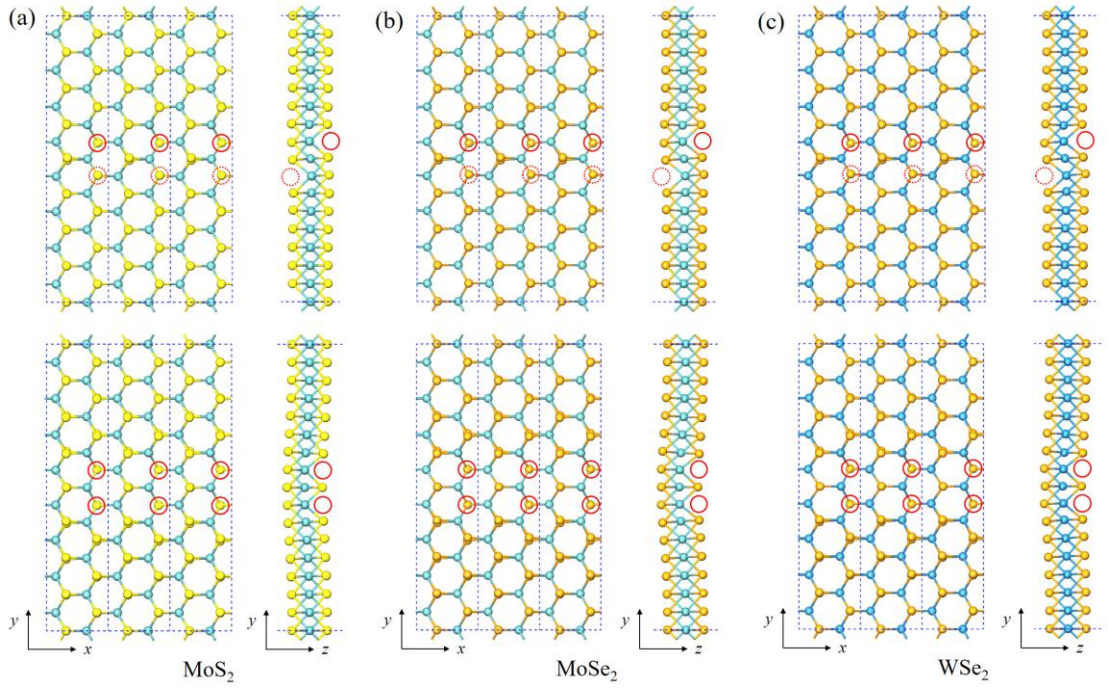

Figure S9. Optimized structures of (a) MoS_2, (b) $MoSe_2$, and (c) WSe_2 with double line defects. The top and bottom panels are DLD-I and DLD-II configurations respectively.

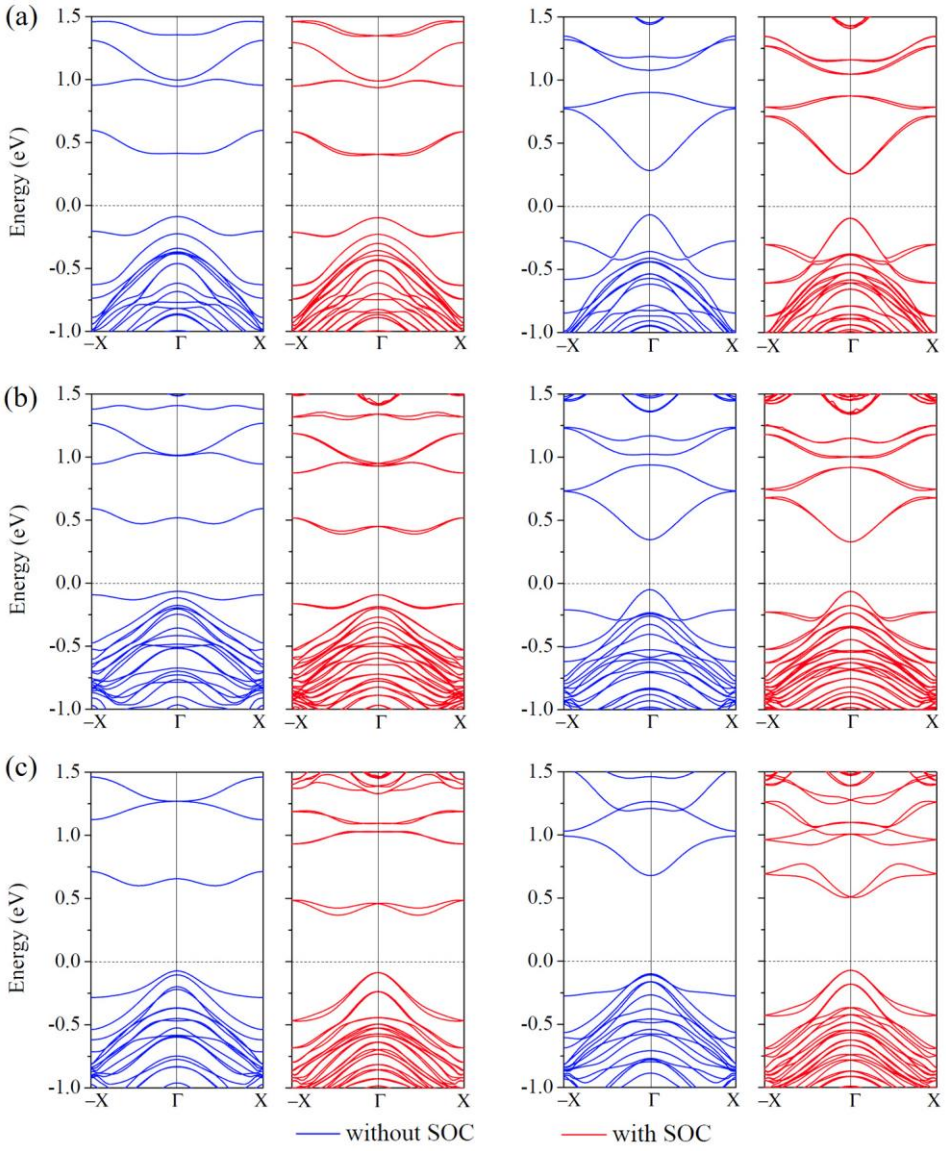

Figure S10. Band structures without and with SOC of (a) MoS_2, (b) $MoSe_2$, and (c) WSe_2 with the DLD-I configuration (the left panels) and the DLD-II configuration (the right panels) respectively.

Table S1. Values of onsite energy ε, hopping parameters t_1 and t_2, SOC parameter α, and lattice constant a in the DLD-I and DLD-II engineered MoS_2, $MoSe_2$ and WSe_2

		ε (eV)	t_1 (eV)	t_2 (eV)	α (eV)	a (Å)
DLD-I	MoS_2	0.469	-0.046	0.015	0.006	5.465
	$MoSe_2$	0.446	-0.020	0.020	0.006	5.681
	WSe_2	0.444	-0.016	0.020	0.015	5.675
DLD-II	MoS_2	0.518	-0.111	-0.022	0.005	5.460
	$MoSe_2$	0.544	-0.092	-0.014	0.003	5.668
	WSe_2	0.688	-0.073	-0.018	0.025	5.661

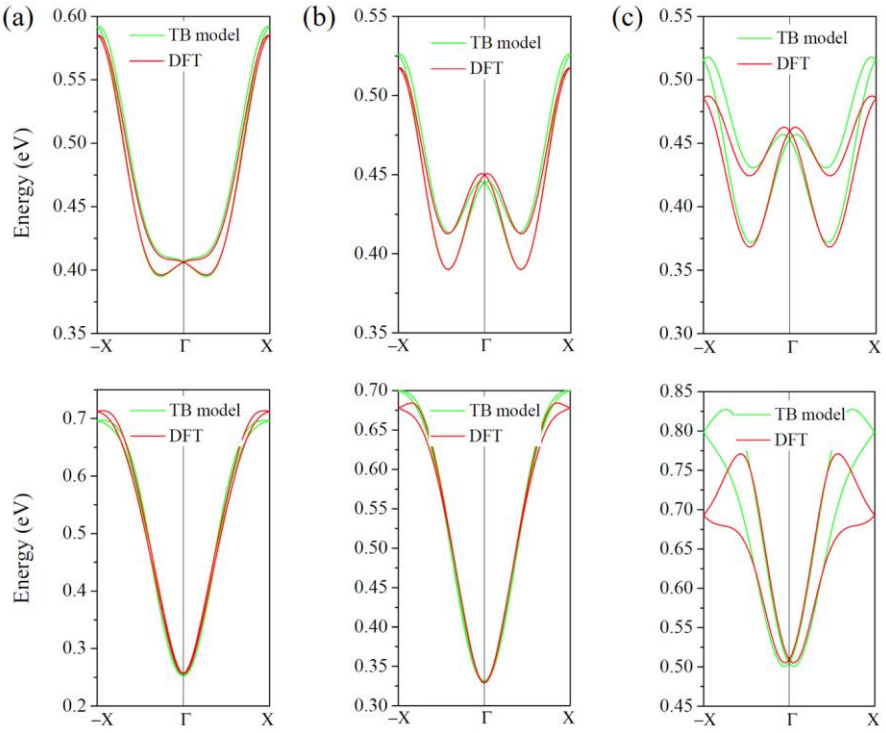

Figure S11. Comparison of band structures obtained using TB model and DFT calculations for (a) MoS_2, (b) $MoSe_2$ and (c) WSe_2 with the DLD-I configuration (the top panels) and the DLD-II configuration (the bottom panels) respectively.

To protect the PSH states from being removed by chemical passivation when exposed to air, one promising way is to sandwich the DLD engineered TMDs between two sheets (like BN) with a large band gap, as illustrated in Figure S12a. To confirm

the feasibility, we calculate the band alignment of the BN monolayer and the DLD engineered TMDs, and summarize the results in Figure S12b. It shows that the proposed PSH states are all inside the band gap of the BN monolayer, indicating that when the DLD engineered TMDs are sandwiched between two BN monolayers, the PSH states will be isolated from other states.

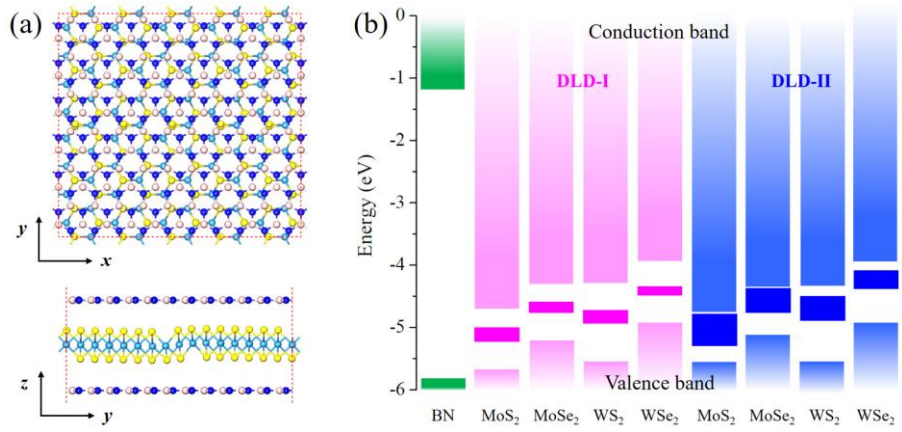

Figure S12. (a) Top and side views of the DLD engineered TMD encapsulated in the BN monolayers. Here the DLD-I engineered WS_2 is used as an illustration. (b) Band alignment of the BN monolayer and the DLD engineered TMDs. The mid-gap states of the DLD engineered TMDs mark the positions of the ideal PSH states in the present study. The vacuum energies are set to zero when calculating the band alignment diagrams.

For comparison, we also calculate band structure and corresponding spin components of pristine WS_2 in the primitive cell, the minimum rectangular cell (containing six atoms) and the supercell with the same lattice constants of that used in Figure 2. The latter two are actually the Brillouin zone folding of the primitive cell. We plot the structure and the corresponding Brillouin zone of the three cells in Figure S13, and the calculated spin-projected band structures in Figure S14.

Figure S14a shows the results of the primitive cell, where bands along the Γ-M path are spin degenerate, while those along the Γ-K and M-K paths are split with spin vectors all along ***z*** direction. The unique spin splitting is attributed to the C_{3v} symmetry

and 2D nature of pristine WS_2.[4] As for other two cells, their band structures in Figure S14b-c result from the band folding of the primitive cell with unaltered spin components since no symmetry breaking occurs during the folding process.

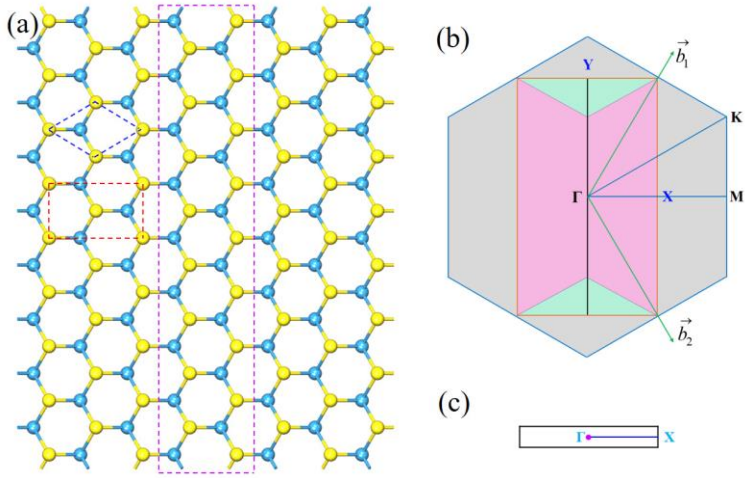

Figure S13. (a) Structure of pristine WS_2. Blue, red and purple dashed lines represent the primitive cell, the six-atom rectangular cell, and the supercell with the same lattice constants as that used in Figure 2 of the main text, respectively. (b) The Brillouin zone of the primitive cell (hexagon) and the six-atom rectangular cell (rectangle). (c) The Brillouin zone of the supercell with the same lattice constants as that used in Figure 2 of the main text.

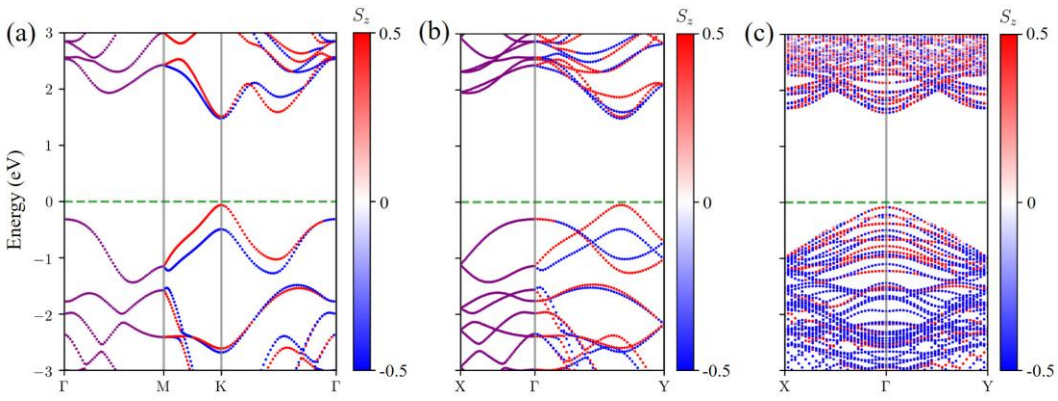

Figure S14. Spin-projected band structures of WS_2 for (a) the primitive cell, (b) the six-atom rectangular cell and (c) the supercell with the same lattice constants as that used in Figure 2 of the main text. Color bars represent expectation values of S_z and the purple dashed lines are spin degenerate bands.

(1) Vajna, S.; Simon, E.; Szilva, A.; Palotas, K.; Ujfalussy, B.; Szunyogh, L. *Phys. Rev. B* **2012,** *85*, 075404.
(2) Kepenekian, M.; Robles, R.; Katan, C.; Sapori, D.; Pedesseau, L.; Even, J. *ACS Nano* **2015,** *9*, 11557-11567.
(3) Barja, S.; Wickenburg, S.; Liu, Z.-F.; Zhang, Y.; Ryu, H.; Ugeda, Miguel M.; Hussain, Z.; Shen, Z.-X.; Mo, S.-K.; Wong, E.; Salmeron, Miquel B.; Wang, F.; Crommie, M. F.; Ogletree, D. F.; Neaton, Jeffrey B.; Weber-Bargioni, A. *Nat. Phys.* **2016,** *12*, 751.
(4) Zhu, Z. Y.; Cheng, Y. C.; Schwingenschlögl, U. *Phys. Rev. B* **2011,** *84*, 153402.